

Article

Study on a Mixed-Cation Halide Perovskite-Based Deep-Ultraviolet Photodetector

Ga In Choi , Chung Wung Bark  and Hyung Wook Choi * 

Department of Electrical Engineering, Gachon University, Seongnam-si 13120, Republic of Korea

* Correspondence: chw@gachon.ac.kr; Tel.: +82-31-750-5562

Abstract: Deep-ultraviolet (UV) sensing has attracted significant interest because of its wide range of applications. A mixed-cation halide perovskite-based photodetector prepared by mixing $\text{CH}_3\text{NH}_3\text{PbX}_3$ ($X = \text{I}, \text{Br}, \text{and Cl}$) and $\text{HC}(\text{NH}_2)\text{PbX}_3$ ($X = \text{I}, \text{Br}, \text{and Cl}$) exhibits high stability and excellent light absorption. In this study, perovskite was prepared by mixing CH_3NH_3^+ (FA^+) and $\text{HC}(\text{NH}_2)_2^+$ (MA^+) cations using I^- , Br^- , and Cl^- halide anions. The bandgaps of the prepared perovskites increased to 1.48, 2.25, and 2.90 eV with I-, Br-, and Cl-, respectively, and the light absorption spectra shifted to shorter wavelengths. An increase in the redshift of the light absorption led to an increase in the photocurrent. The FAPbCl_3 - MAPbCl_3 -based photodetector showed a high responsivity of 5.64 mA/W, a detectivity of 4.03×10^{11} , and an external quantum efficiency of 27.3%. The results suggested that the FAPbCl_3 - MAPbCl_3 perovskite is suitable for deep-UV light sensing and is an excellent candidate for the fabrication of a sensitive photodetector.

Keywords: mixed-cation; halide perovskite; perovskite thin film; UVC sensor; photodetector

1. Introduction

A photodetector converts light into electricity. It has excellent sensitivity compared to other detectors, owing to the detection method using light [1]. Ultraviolet (UV) photodetectors have been applied in various fields over the past few years, including the image detection, military, medical, environmental, and communication fields, and have attracted considerable attention [2]. In general, UV light constitutes approximately 10% of the electromagnetic waves emitted from the sun and can be classified into three types based on the wavelength range—UVA: 320–400 nm, UVB: 280–320 nm, and UVC: 180–200 nm [3]. The UVC emitted by the sun is mostly absorbed by the ozone layer. However, it is also emitted by artificial light sources such as partial discharges from power equipment, arc welding torches, and mercury lamps [2]. In addition to adversely affecting the human body and causing skin cancer and cataracts, UVC can also cause accidents in industrial facilities [4,5]. Therefore, to prevent damage from UVC, UVC photodetectors are used in such facilities. They are also used in scientific research for applications in fire detection, remote control, secure communication, and chemical and biological analyses [6]. A typical example is installing UVC photodetectors in switchboards to prevent fire accidents caused by arc flashes in power facilities [7]. Therefore, it is essential to develop a detector capable of detecting UVC to prevent damage caused by UVC.

Previously, materials such as organic polymers, silicon, III-V compounds, and colloidal quantum dots were used for photodetector fabrication [1,8]. However, silicon has a narrow bandgap; therefore, silicon-based photodetectors require the installation of a separate UV filter. Silicon-based photodetectors also exhibit a low fabrication efficiency and require high-vacuum conditions [9]. Further, the fabrication of a high-performance colloidal quantum dots-based detector is difficult because of the short carrier diffusion length of colloidal quantum dots. They are also expensive and require high temperatures and complicated processes [10,11]. Perovskites have attracted attention as a suitable alternative for existing



Citation: Choi, G.I.; Bark, C.W.; Choi, H.W. Study on a Mixed-Cation Halide Perovskite-Based Deep-Ultraviolet Photodetector. *Coatings* **2023**, *13*, 248. <https://doi.org/10.3390/coatings13020248>

Academic Editor: Peng Yu

Received: 27 December 2022

Revised: 16 January 2023

Accepted: 17 January 2023

Published: 20 January 2023



Copyright: © 2023 by the authors. Licensee MDPI, Basel, Switzerland. This article is an open access article distributed under the terms and conditions of the Creative Commons Attribution (CC BY) license (<https://creativecommons.org/licenses/by/4.0/>).

detector materials due to their excellent properties such as significant light absorption, a long carrier spread length, and an adjustable bandgap [12]. In addition, the solution processing of perovskite is inexpensive because it is a simple process that can be conducted at low temperatures [13,14].

Perovskites have an ABX_3 chemical structure. There are cations such as formamidinium ($CH(NH_2)_2PbX_3$, FA), methylammonium (CH_3NH_3 , MA), cesium (Cs), rubidium (Rb) that correspond to the A position in organic–inorganic lead halide perovskite [15,16]. In addition, pyrrolidine (Py, C_4H_8NH) and MoS_2 have been reported as candidates for perovskite materials [17–19]. In general, formamidinium lead halide ($FAPbX_3$) and methylammonium lead iodide ($MAPbX_3$) are used as perovskite materials, and studies are being conducted to mix MA and FA to compensate for the shortcomings of perovskites and increase their stability [20]. The improved electrical properties of mixed cations have been demonstrated in several studies [21,22].

It is essential to adjust the bandgap to allow the UVC photodetector to absorb a short wavelength of 254 nm because the wavelength of UVC light is in the range of 200–280 nm. The wavelength that exhibits the strongest light absorption depends on the bandgap. This means the detection selectivity of the photodetector can be determined by adjusting the bandgap of the material.

In this study, the bandgap energy, detection selectivity, and photoresponse characteristics of $FAPbX_3$ - $MAPbX_3$ ($X = I, Br, \text{ and } Cl$) photodetectors fabricated using mixed cations were investigated in the UVC region.

2. Materials and Methods

2.1. Materials

The following materials and chemicals were used: A quartz-glass substrate with a 160 nm-thick layer of indium tin oxide (ITO) was obtained from TMA (Seoul, Republic of Korea). Formamidinium iodide (FAI), methylammonium iodide (MAI), formamidinium bromide (FABr), methylammonium bromide (MABr), formamidinium chloride (FACl), and methylammonium chloride (MACl) were purchased from GreatCell Solar (Queanbeyan, Australia). Lead (II) iodide (99.999%), N,N-dimethylformamide (DMF, 99.8%), dimethyl sulfoxide (DMSO, 99.7%), toluene (99.8%), sodium dodecylbenzenesulfonate (SDBS), and 2-propanol (IPA, 75 wt.%) were purchased from Sigma-Aldrich (St. Louis, MO, USA). A SnO_2 colloidal solution (15 wt.% in water) was purchased from Alfa Aesar (Seoul, Republic of Korea). All the materials were used without further purification.

2.2. Methods

Figure 1a shows a schematic of the structure of a mixed cation-based n-i-p UVC photodetector, and Figure 1b shows the fabrication process. To remove the organic matter, the ITO quartz substrate was ultrasonically cleaned using a neutral detergent, water, acetone, ethanol, and distilled water for 20 min each. After drying in an oven at 80 °C for 20 min, a UV–ozone treatment was performed for 30 min to further remove moisture. A polymer tape was applied to the cleaned substrate to cover a portion of the ITO, and PH1000 was deposited using spin coating. To reduce the sheet resistance and increase the transmittance in the UV region, a methanol post-treatment was performed based on a previously reported procedure [23]. After depositing the front electrode, SnO_2 was deposited as an electron transport layer. Next, 1.2 mL of the SnO_2 colloidal solution (15 wt.%), 5.2 mL of deionized water, and 1 mg of SDBS were used to prepare a SnO_2 –SDBS mixed solution. The SnO_2 colloidal solution was spin-coated at 3000 rpm for 20 s and then annealed at 150 °C for 30 min. A two-step spin coating method was employed for the perovskite layer. First, 1.4 mol of 92.5% $FAPbX_3$ was spin-coated at 4000 rpm for 20 s and then annealed at 150 °C for 15 min to form a part of the perovskite. After sufficient cooling, MAX/IPA was spin-coated at 4000 rpm for 20 s and then annealed at 100 °C for 20 min. A spiro-OMeTAD hole-transport layer was spin-coated at 4000 rpm for 20 s. Finally, Au was deposited using a thermal evaporator.

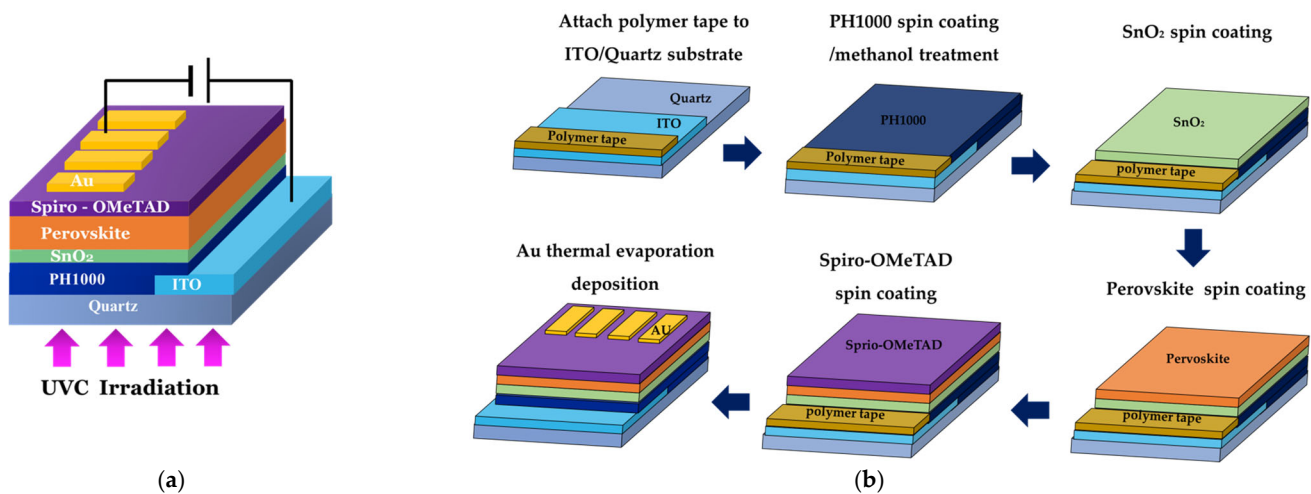


Figure 1. (a) Schematic showing the structure of the mixed cation-based n-i-p UVC photodetector. (b) The fabrication process for the detector.

2.3. Device Characterization

The crystal structure of the perovskite film was investigated using X-ray diffraction (XRD, DMAX 2200, Rigaku, Tokyo, Japan) at a scan rate of $5.00^\circ/\text{min}$. The top surfaces of the perovskite films were observed using scanning electron microscopy (SEM, S-4700, Hitachi, Tokyo, Japan). The light absorbance of the device was measured using UV–visible (UV–vis) spectroscopy (UV-vis 8453, Agilent, Santa Clara, CA, USA). The electrical response of the perovskite photodetector was measured using a combined source and measurement meter (Source Measure Unit, Keithley Instruments, Cleveland, OH, USA) and a UV lamp (6 W, 254 nm) (VL-6.LC, Vilber Lourmat, Marne-la-Vallée, France) under 254, 302, and 356 nm irradiations.

3. Results and Discussion

The crystallinities of the $\text{FAPbX}_3\text{-MAPbX}_3$ ($x = \text{I, Br, and Cl}$) films were investigated by measuring the XRD patterns. In Figure 2a, the major perovskite diffraction peaks are present at $2\theta = 14.1^\circ$ and 29.4° for $\text{FAPbI}_3\text{-MAPbI}_3$, 14.9° and 30.1° for $\text{FAPbBr}_3\text{-MAPbBr}_3$, and 15.6° and 31.5° for $\text{FAPbCl}_3\text{-MAPbCl}_3$, corresponding to the (100) and (200) planes, respectively. When $X = \text{I, Br, and Cl}$, all three major peaks gradually shift to the left, which is due to a decrease in the lattice spacing, difference in the ion sizes of the materials, and difference in the crystal structure sizes resulting from the different lattice constants [24,25]. The three X anions had ionic sizes of 2.2 (I^-), 1.96 (Br^-), and 1.81 Å (Cl^-) [26]. When X is I, the lattice constants were $a = b = 8.83$ Å and $c = 12.69$ Å in the tetragonal system, and when X was Br or Cl, they were 5.92 Å and 5.67 Å, respectively [26]. These values correspond to a cubic system with different lattice constants. Therefore, when X was Br or Cl, similar XRD patterns were observed [25]. Other small XRD peaks are also observed, which are inferred to originate from residual MACl and PbI_2 [24,25]. However, in Figure 3a–c, no large residue was observed in the SEM picture of the surface, and the XRD result showed a much smaller peak size than that of the perovskite phase. Although small peaks other than perovskite peaks were commonly reported in previous studies of mixed cation perovskites, small rises in peaks other than the perovskite peak do not significantly affect performance [27–29].

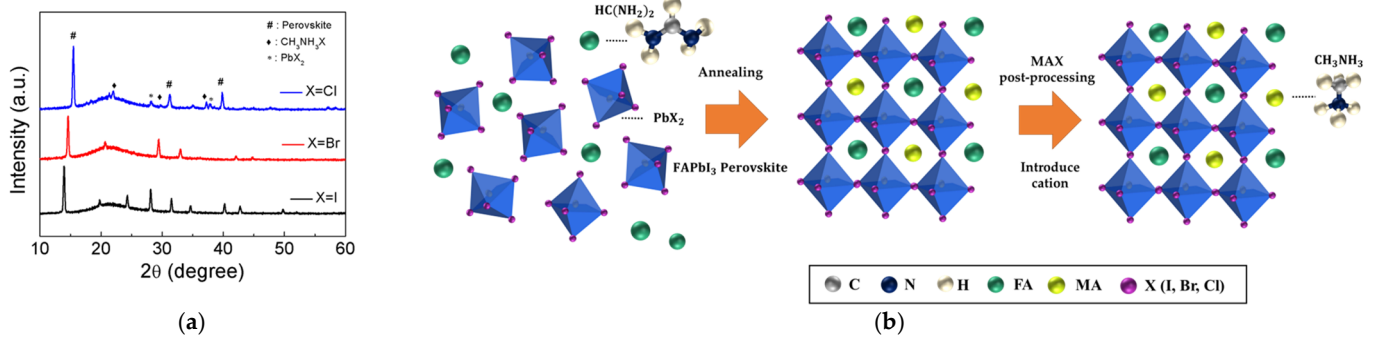


Figure 2. (a) XRD pattern of the FAPbX₃-MAPbX₃ (X = I, Br, and Cl) films, (b) Schematic of mixed cation halide perovskite for incorporation of cations.

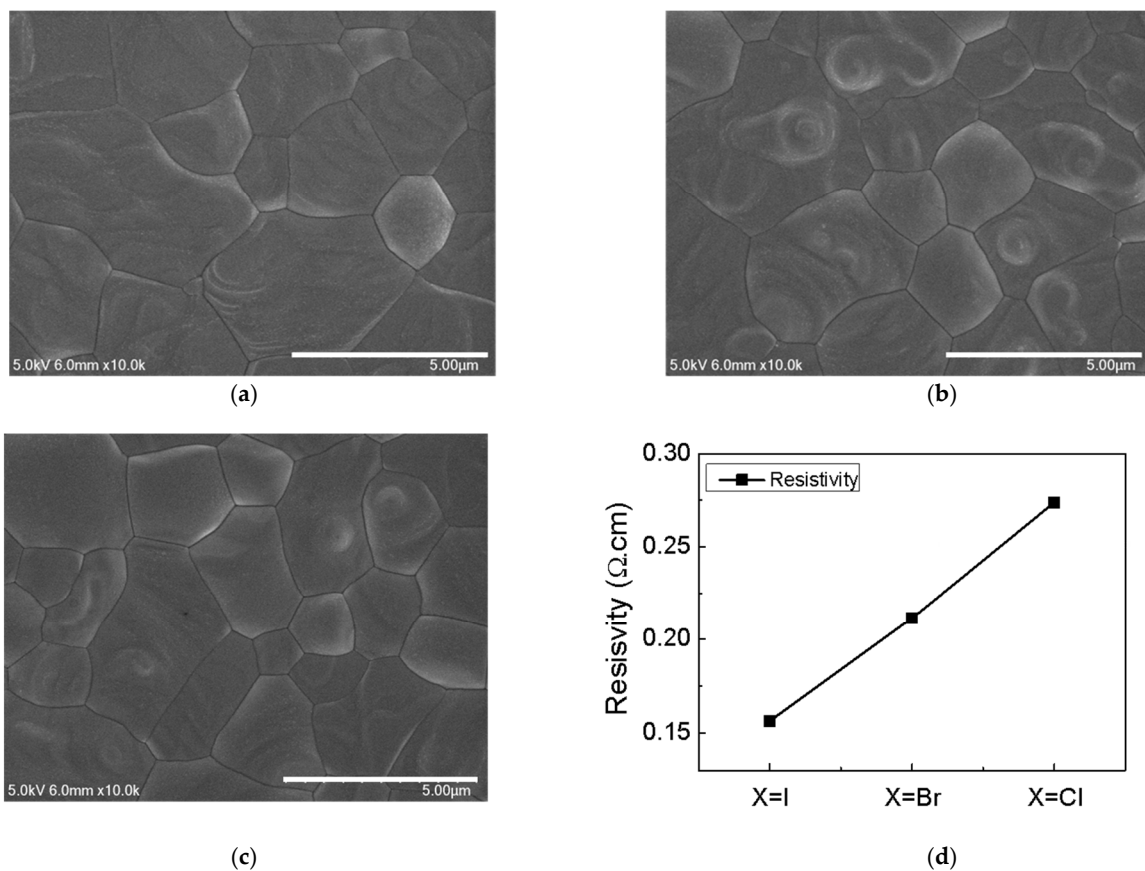


Figure 3. SEM images of the FAPbX₃-MAPbX₃ (X = I, Br, and Cl) thin film surfaces for (a) X = I, (b) X = Br, and (c) X = Cl, and (d) resistivity.

Figure 2b shows the formation mechanism for the mixed-cation halide perovskite. First, 92.5 mol% FAPbX₃ is deposited as an intermediate complex. After the process of post-treatment with MAX, MA is introduced as a cation to form a mixed cation. As a result of the cation mixing, a mixed-cation perovskite without an unstable δ -FAPbX₃ phase is formed.

The SEM images of the surface of the perovskite thin film are shown in Figure 3a–c. The average domain diameters are 3.41, 2.69, and 2.55 μm for perovskites with X = I, Br, and Cl, respectively. The grain size was averaged by measuring the domain diameter more than 100 times using the Image J program. The differences in the average diameters are caused by the differences in the sizes of I[−] (2.2 Å), Br[−] (1.96 Å), and Cl[−] (1.81 Å) [24]. Although a smaller grain size is observed when X = Br or Cl, compared to that when X = I,

all three films show dense and clear surfaces without pinholes or defects. Therefore, it can be inferred that the perovskite is well formed.

Figure 3d shows the resistivity values of $\text{FAPbX}_3\text{-MAPbX}_3$ ($X = \text{I, Br, and Cl}$), as measured using the Hall effect. The resistivity has small values in the order of $X = \text{I, Br, and Cl}$. The increase in resistivity is due to an increase in the light absorption and a decrease in grain size [30,31]. When the light absorption increases, the photodetector benefits but the resistivity increases because of carrier scattering [32]. The resistivity of $\text{FAPbCl}_3\text{-MAPbCl}_3$ is approximately $0.12 \Omega\cdot\text{cm}$ greater than that of $\text{FAPbI}_3\text{-MAPbI}_3$. However, considering the UVC selectivity due to the wider bandgap energy of $\text{FAPbCl}_3\text{-MAPbCl}_3$, this is a small difference as the bandgap energy of the former is approximately twice that of the latter.

Figure 4a shows the light absorption in the UV–vis spectrum. In $\text{FAPbX}_3\text{-MAPbX}_3$ ($X = \text{I, Br, and Cl}$), when X is I, light absorption occurs over a wide band of approximately 200–500 nm. In the case of Br, the absorption occurs at 200–320 nm, and Cl shows a high light absorption in the range of approximately 200–280 nm. A photodetector is characterized by its light detection in a desired wavelength band. UVC photodetectors are developed to detect light in the range of 200–280 nm. $\text{FAPbCl}_3\text{-MAPbCl}_3$ films have a high absorption coefficient in the range of 200–280 nm, enabling the fabrication of a detector for UVC light without a separate filter. Figure 4b shows a bandgap energy based on the light absorption measurements. Based on the light absorption coefficient, the bandgap energy values of $\text{FAPbX}_3\text{-MAPbX}_3$ ($X = \text{I, Br, and Cl}$) are estimated to be approximately 1.48, 2.25, and 2.90 eV, respectively, with the widest bandgap observed when $X = \text{Cl}$. A wide bandgap material is advantageous for fabricating UV photodetectors because it can absorb and emit high-energy photons [29,32]. Therefore, $\text{FAPbCl}_3\text{-MAPbCl}_3$ is suitable for fabricating UVC photodetectors.

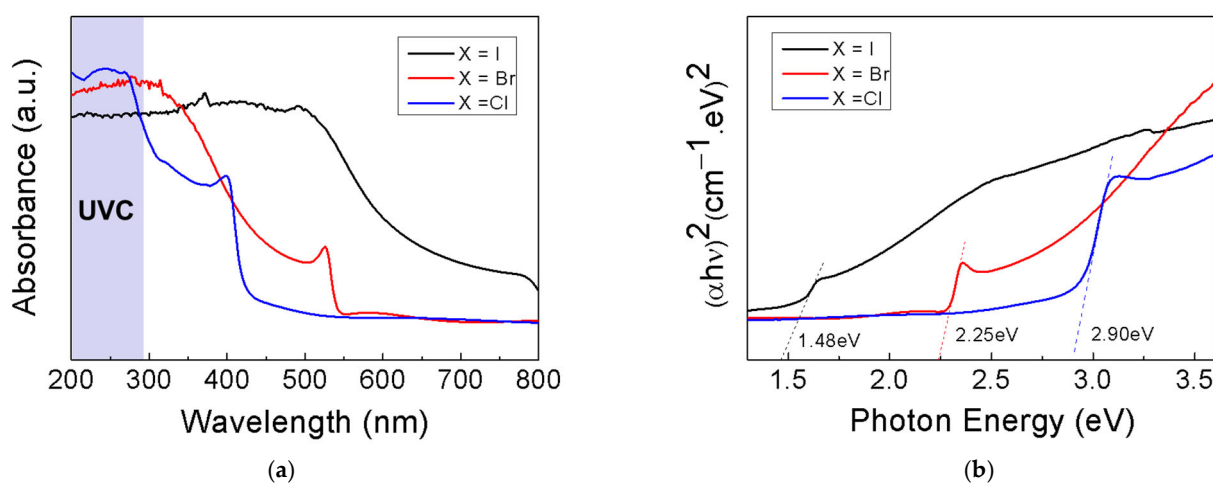


Figure 4. Light absorption and bandgap energy values of $\text{FAPbX}_3\text{-MAPbX}_3$ ($X = \text{I, Br, and Cl}$) thin films. (a) UV-vis spectrum and (b) bandgap energy dependent on light absorption.

Figure 5a–c show current–voltage (I – V) curves to compare the characteristics of the photodetectors based on halide anions. The devices were measured from -1 to $+1$ V at a scan rate of 2.5 V/s, an irradiated light wavelength of 254 nm, and an intensity of 0.648 mW/cm^2 . The dark current was generated in a dark environment without irradiated light, and a smaller value indicated a better the performance for the detector [32]. In Figure 5a–c, the dark current at a 0 V has very small values of 1.05 , 2.82 , and 1.56 μA for $X = \text{I, Br, and Cl}$, respectively. When light at 254 nm is irradiated, the photocurrent has a higher value than the dark current, and the current increases with the voltage because of the photo-generated carriers [2,33]. At a 1 bias, the dark currents of the $\text{FAPbX}_3\text{-MAPbX}_3$ ($X = \text{I, Br, and Cl}$) photodetectors show similar values; however, the photocurrent gradually increases when X is changed from I to Br and Cl, with values of 302.1 , 345.7 , and 393.9 μA , respectively. The smallest photocurrent value is observed when $X = \text{I}$ despite the lower resistivity. This

is because when $X = I$, it has a higher saturation voltage and lower trap density compared to those when $X = Cl$ [25].

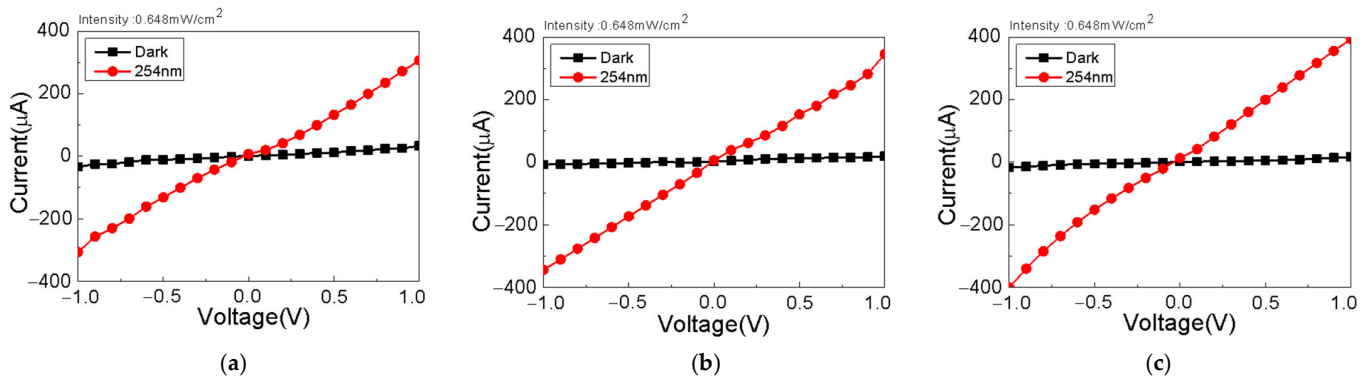


Figure 5. Current–voltage curves of $FAPbX_3$ - $MAPbX_3$ ($X = I, Br,$ and Cl) photodetectors with different halides: (a) $X = I$, (b) $X = Br$, and (c) $X = Cl$.

Wavelength selectivity is an important factor when comparing the performances of photodetectors [33]. To confirm that the photodetector operated only in the UVC region, the I–V curves were examined in the UVA, UVB, and UVC regions. Figure 6a–c shows the photocurrents in each region. In Figure 6a, the values of the three currents are similarly measured. The $FAPbI_3$ - $MAPbI_3$ detector has a wide absorption band of approximately 200–500 nm. Rather, the current value is the highest at 365 nm. Figure 6b shows that the $FAPbBr_3$ - $MAPbBr_3$ detector has strong absorbance in the range of 200–320 nm and high photocurrents in the UVB and UVC regions. The $FAPbCl_3$ - $MAPbCl_3$ detector exhibits strong absorbance in the range of 200–280 nm, and it shows a high photocurrent at 254 nm, corresponding to UVC. The photocurrent decreases with an increase in the light wavelength, as shown in Figure 6c. These results suggest that among the analyzed detectors, the $FAPbCl_3$ - $MAPbCl_3$ detector is the most suitable for UVC detection.

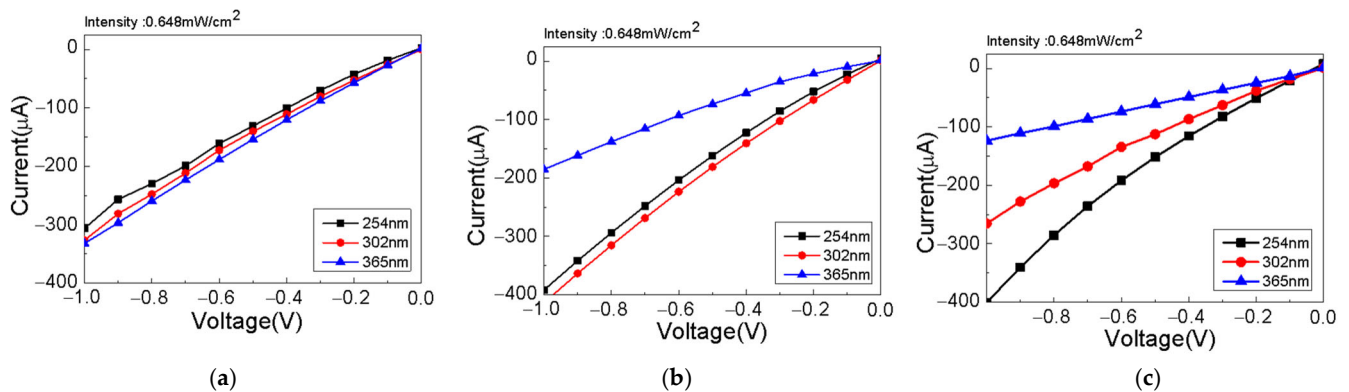


Figure 6. Current–voltage curves of $FAPbX_3$ - $MAPbX_3$ ($X = I, Br,$ and Cl) photodetectors at different wavelengths of light: (a) $X = I$, (b) $X = Br$, and (c) $X = Cl$.

The parameters of each detector were compared to investigate the detector performance for halide material. The significant parameters that determined the detector performance included the responsivity (R), detectivity (D^*), and external quantum efficiency (EQE). The responsivity was calculated as follows:

$$R = \frac{I_{254} - I_{dark}}{P \cdot S},$$

where I_{254} is the photocurrent; I_{dark} is the current in a dark environment; P is the power of the irradiated light; and S is the area receiving the light.

The detectivity refers to the smallest signal that can be detected using a detector and is affected by the responsivity and dark current. It is defined as follows [2]:

$$D^* = \frac{R}{\sqrt{2qJ_{dark}}},$$

where R is the responsivity; q is the electron charge; and J_{dark} is the dark current density, which is the value of the dark current per unit area. The detectivity indicates that the dark current is an important factor in determining the photodetector performance. Figure 7a shows the responsivity values of the FAPbX₃-MAPbX₃ (X = I, Br, and Cl) photodetectors from 0 to 1 V when 254 nm light was irradiated with an intensity of 0.648 mW/cm². At a 0 bias, the detector shows responsivity of 3.83, 4.70, and 5.60 mA/W for X = I, Br, and Cl, respectively. As the bias increases, the responsivity also increases to 161.78, 197.06, and 223.77 mA/W at a 1 bias for X = I, Br, and Cl, respectively. This is because the internal electric field increases with the bias voltage, which suppresses carrier recombination and increases the photon-to-charge conversion efficiency [34]. In Figure 7b, the detectivity values of the FAPbX₃-MAPbX₃ (X = I, Br, and Cl) photodetectors are 3.37×10^{11} , 2.52×10^{11} , and 4.04×10^{11} at a bias of 0 V, respectively. As the voltage increases from 0 to 1 V, the detectivity also increases, which is similar to the responsivity results, because the detectivity is related to the responsivity and dark current. These results indicate that among the FAPbX₃-MAPbX₃ (X = I, Br, and Cl) detectors, the FAPbCl₃-MAPbCl₃ detector is the most sensitive at 254 nm.

Figure 7c shows the on/off ratios of the FAPbX₃-MAPbX₃ (X = I, Br, and Cl) detectors from 0 to 1 V. The on/off ratio is an important performance characteristic of photodetectors [35]. The on-off ratio shows the highest value when X is Cl. Figure 7d displays the measurements of the instantaneous changes in current by repeating the detector on/off cycle. The irradiated light had a wavelength of 254 nm and an intensity of 0.648 mW/cm² at a 1 bias. The detector responses can be compared with the increases in photocurrent, and among the FAPbX₃-MAPbX₃ (X = I, Br, and Cl) detectors, FAPbCl₃-MAPbCl₃, which has the highest optical absorption at 245 nm, shows the highest increase in current. Figure 7e shows the response time. In general, the response time is measured based on the current change in the range of 10–90%; however, in this study, the comparison was conducted in the range of 50–90%. Although the response time is the shortest for the FAPbI₃-MAPbI₃ photodetector, the FAPbI₃-MAPbI₃ detector has a wide light absorption band of 200–500 nm, along with higher photocurrents in the UVA and UVB wavelength bands than that measured for UVC. This shows that the FAPbI₃-MAPbI₃ detector has inappropriate selectivity in the UVC region despite its fast response speed. The FAPbBr₃-MAPbBr₃ and FAPbCl₃-MAPbCl₃ detectors have a response time difference of less than 0.06 s compared to the FAPbI₃-MAPbI₃ detector. This means all three detectors show sensitive responses with small differences when the increase in photocurrent is considered. Figure 7f shows the on/off switching repeatability of the FAPbCl₃-MAPbCl₃ photodetector. The on/off switching was investigated for 1000 s by repeating the on/off cycle 100 times at 254 nm with an intensity of 0.648 mW/cm². The current remains constant from approximately 80 to 840 s. Subsequently, it slightly decreases; however, the photocurrent is maintained for a relatively long period, which confirms the reproducibility. Stability is an important factor for the operation of a perovskite device [36]. Nguyen and coworkers have fabricated a UVC photodetector that maintains a fast response speed even after storage for three weeks in ambient air [2]. The fabrication of the FAPbCl₃-MAPbCl₃ photodetector is expected to have similar stability because the photodetector was fabricated under the same conditions and materials as in Nguyen's study.

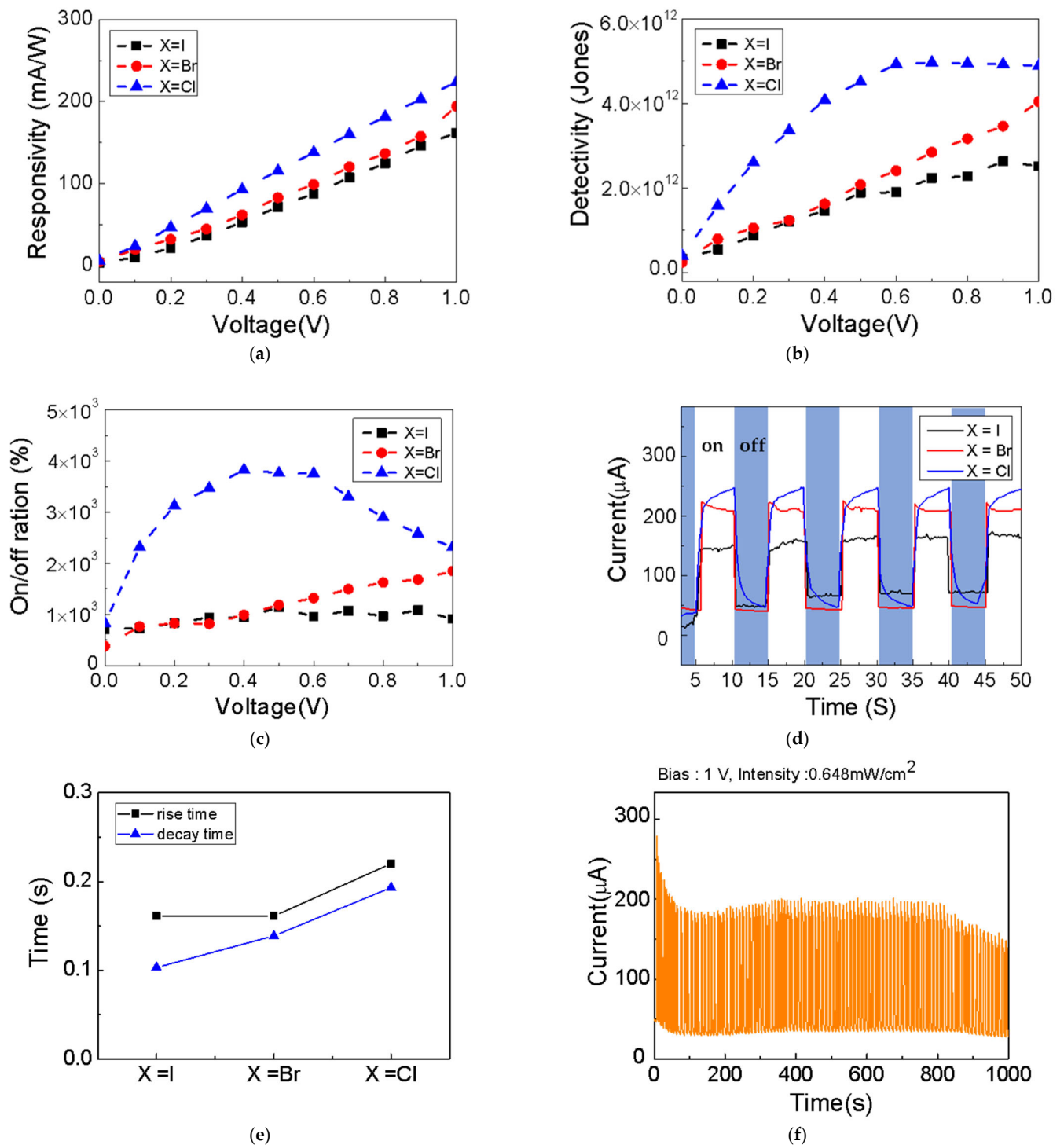


Figure 7. Responses of the FAPbX₃-MAPbX₃ (X = I, Br, and Cl) detectors: (a) responsivity; (b) detectivity; (c) on/off ratio; (d) transient photoresponse through repeated on/off cycles; (e) detector response time, rise-time, and decay-time; and (f) switching of detectors to investigate photostability.

Table 1 lists the parameters of the various UVC photodetectors fabricated using perovskite materials. The responsivity, detectivity, and EQE values are compared. The EQE is the ratio of the number of incident photons to the number of electrons produced [37]:

$$EQE = \frac{Rhc}{e\lambda},$$

where R is the responsivity; h is Planck's constant; c is the speed of light; and λ is the wavelength of the incident light. The EQE is related to the speed at which photons are converted from electrons to electrons/holes [2,38]. The fabricated FAPbCl₃-MAPbCl₃ photodetector shows a responsivity of 5.64 mA/W and detectivity of 4.03×10^{11} , which implies that it is more sensitive than those reported in other studies. In addition, it has an EQE of 27.3%, which is higher than those of perovskite-based photodetectors developed in other studies. These results indicate that FAPbCl₃-MAPbCl₃ is an excellent material for the development of UVC photodetectors.

Table 1. Parameter comparison of UVC photodetectors based on various halide perovskites.

Materials	Light (nm)	Bias (V)	R (mA/W)	D^* (Jones)	EQE (%)	Ref.
(FAPbCl ₃) _{1-x} (MAPbCl ₃) _x	254	0	5.60	4.03×10^{11}	27.3	[This study]
(FAPbI ₃) _{1-x} (MAPbBr ₃) _x	254	0	4.92	7.57×10^{10}	-	[35]
MAPbBr ₃	254	2	4.57	1.02×10^{13}	22.2	[5]
Cu ₃ Cu ₂ I ₅	265	0	0.11	6.9×10^{11}	-	[39]
CsPbBr ₃	254	2	0.24	1.1×10^9	0.05	[23]
CaSnO ₃	255	0	2.25	1.56×10^{10}	1.06	[40]
Diamond/ β -Ga ₂ O ₃	244	0	0.2	6.9×10^9	-	[41]
Mn _{0.52} Zn _{0.48} O ₃	250	10	0.1	-	-	[11]
Nb:SrTiO ₃ /Ga ₂ O ₃	254	0	2.6	-	1.3	[42]
ZnO-Ga ₂ O ₃	254	-2	9.7	-	-	[43]

4. Conclusions

In summary, mixed-cation-based halide perovskite UVC photodetectors were fabricated using a simple and low-temperature process, and the photodetector characteristics of different halide materials were compared. The band gap energies of FAPbX₃-MAPbX₃ perovskite with X = I, Br, and Cl were 1.48, 2.25, and 2.90 eV, respectively. The FAPbCl₃-MAPbCl₃ photodetector showed a high absorbance only in the UVC region, which demonstrated that it had appropriate selectivity for UVC detection. At a 0 bias, the FAPbCl₃-MAPbCl₃ photodetector showed a sensitive response, exhibiting a responsivity of 5.64 mA/W, a detectivity of 4.03×10^{11} , and an EQE of 27.3%. These results suggested that FAPbCl₃-MAPbCl₃ perovskite, which has a wide bandgap, could be an excellent material for fabricating UVC photodetectors.

Author Contributions: Investigation, G.I.C.; Validation, C.W.B. and H.W.C.; Writing—original draft preparation, G.I.C.; Writing—review and editing, G.I.C., C.W.B. and H.W.C.; Supervision, H.W.C. All authors have read and agreed to the published version of the manuscript.

Funding: This research was supported by the Basic Science Research Capacity Enhancement Project through a Korea Basic Science Institute (National Research Facilities and Equipment Center) grant funded by the Ministry of Education (2019R1A6C1010016). This work was supported by a Korea Institute for Advancement of Technology (KIAT) grant funded by the Korea Government (MOTIE) (P0012451, The Competency Development Program for Industry Specialist).

Institutional Review Board Statement: Not applicable.

Informed Consent Statement: Not applicable.

Data Availability Statement: The data are available upon reasonable request from the corresponding author.

Conflicts of Interest: The authors declare no conflict of interest.

References

1. Leung, S.F.; Ho, K.T.; Kung, P.K.; Hsiao, V.K.S.; Alshareef, H.N.; Wang, Z.L.; He, J.H. A self-powered and flexible organometallic halide perovskite photodetector with very high detectivity. *Adv. Mater.* **2018**, *30*, 1704611. [[CrossRef](#)] [[PubMed](#)]
2. Nguyen, T.M.H.; Kim, S.; Bark, C.W. Solution-processed and self-powered photodetector in vertical architecture using mixed-halide perovskite for highly sensitive UVC detection. *J. Mater. Chem. A* **2021**, *9*, 1269. [[CrossRef](#)]

3. Park, T.; Hur, J. Self-powered low-cost UVC sensor based on organic-inorganic heterojunction for partial discharge detection. *Small* **2021**, *17*, 2100695. [[CrossRef](#)] [[PubMed](#)]
4. Dixon, A.J.; Dixon, B.F. Ultraviolet radiation from welding and possible risk of skin and ocular malignancy. *Med. J. Aust.* **2004**, *181*, 155–157. [[CrossRef](#)] [[PubMed](#)]
5. Shin, S.G.; Bark, C.W.; Choi, H.W. Study on Performance Improvements in Perovskite-Based Ultraviolet Sensors Prepared Using Toluene Antisolvent and CH₃NH₃Cl. *Nanomaterials* **2021**, *11*, 1000. [[CrossRef](#)]
6. Wu, Z.; Jiao, L.; Wang, X.; Guo, D.; Li, W.; Li, L.; Huang, F.; Tang, W. A self-powered deep-ultraviolet photodetector based on an epitaxial Ga₂O₃/Ga: ZnO heterojunction. *J. Mater. Chem. C* **2017**, *5*, 8688–8693. [[CrossRef](#)]
7. Riba, J.R. Application of Image Sensors to Detect and Locate Electrical Discharges: A Review. *Sensors* **2022**, *22*, 5886. [[CrossRef](#)]
8. Li, C.; Ma, Y.; Xiao, Y.; Shen, L.; Ding, L. Advances in perovskite photodetectors. *InfoMat* **2020**, *2*, 1247–1256. [[CrossRef](#)]
9. Qin, Y.; Long, S.; Dong, H.; He, Q.; Jian, G.; Zhang, Y.; Hou, X.; Tan, P.; Zhang, Z.; Lv, H.; et al. Review of deep ultraviolet photodetector based on gallium oxide. *Chin. Phys. B* **2019**, *28*, 018501. [[CrossRef](#)]
10. Gomes, C.C.; Preto, S. Artificial intelligence and interaction design for a positive emotional user experience. In *Proceedings of the 1st International Conference on Intelligent Human Systems Integration (IHSI 2018): Integrating People and Intelligent Systems*; Dubai, United Arab Emirates, 7–9 January 2018; Advances in Intelligent Systems and Computing; Karwowski, W., Ahram, T., Eds.; Springer: Cham, Switzerland, 2018; Volume 722, pp. 62–68.
11. Ju, Z.G.; Shan, C.X.; Jiang, D.Y.; Zhang, J.Y.; Yao, B.; Zhao, D.X.; Sheen, D.Z.; Fan, X.W. Mg_xZn_{1-x}O-based photodetectors covering the whole solar-blind spectrum range. *Appl. Phys. Lett.* **2008**, *93*, 173505. [[CrossRef](#)]
12. Li, Y.; Shi, Z.F.; Li, X.J.; Shan, C.X. Photodetectors based on inorganic halide perovskites: Materials and devices. *Chin. Phys. B* **2019**, *28*, 017803. [[CrossRef](#)]
13. Dkhissi, Y.; Huang, F.; Rubanov, S.; Xiao, M.; Bach, U.; Spiccia, L.; Caruso, R.A.; Cheng, Y.B. Low temperature processing of flexible planar perovskite solar cells with efficiency over 10%. *J. Power Sources* **2015**, *278*, 325–331. [[CrossRef](#)]
14. Petrov, A.A.; Belich, N.A.; Grishko, A.Y.; Stepanov, N.M.; Dorofeev, S.G.; Maksimov, E.G.; Shevilkov, A.V.; Zakeeruddin, S.M.; Graetzel, M.; Tarasov, A.; et al. A new formation strategy of hybrid perovskites via room temperature reactive polyiodide melts. *Mater. Horizons* **2017**, *4*, 625–632. [[CrossRef](#)]
15. Kubicki, D.J.; Prochowicz, D.; Hofstetter, A.; Zakeeruddin, S.M.; Gratzel, M.; Emsley, L. Phase segregation in Cs-, Rb- and K-doped mixed-cation (MA)_x(FA)_{1-x}PbI₃ hybrid perovskites from solid-state NMR. *J. Am. Chem. Soc.* **2017**, *139*, 14173–14180. [[CrossRef](#)]
16. Hu, Y.; Ayguler, M.F.; Petrus, M.L.; Bein, T.; Docampo, P. Impact of rubidium and cesium cations on the moisture stability of multiple-cation mixed-halide perovskites. *ACS Energy Lett.* **2017**, *2*, 2212–2218. [[CrossRef](#)]
17. Xu, A.F.; Wang, R.T.; Yang, L.W.; Jarvis, V.; Britten, J.F.; Xu, G. Pyrrolidinium lead iodide from crystallography: A new perovskite with low bandgap and good water resistance. *Chem. Commun.* **2019**, *55*, 3251–3253. [[CrossRef](#)] [[PubMed](#)]
18. Wang, H.P.; Li, S.; Liu, X.; Shi, Z.; Fang, X.; He, J.H. Low-dimensional metal halide perovskite photodetectors. *Adv. Mater.* **2021**, *33*, 2003309. [[CrossRef](#)] [[PubMed](#)]
19. Xu, F.; Li, Y.; Liu, N.; Han, Y.; Zou, M.; Song, T. 1D perovskitoid as absorbing material for stable solar cells. *Crystals* **2021**, *11*, 241. [[CrossRef](#)]
20. Mateen, M.; Arain, Z.; Liu, C.; Yang, Y.; Liu, X.; Ding, Y.; Shi, P.; Ren, Y.; Wu, Y.; Dai, S.; et al. High-Quality (FA)_x(MA)_{1-x}PbI₃ for Efficient Perovskite Solar Cells via a Facile Cation-Intermixing Technique. *ACS Sustain. Chem. Eng.* **2019**, *7*, 11760–11768. [[CrossRef](#)]
21. Guo, X.; Ngai, K.; Qin, M.; Lu, X.; Xu, J.; Long, M. The compatibility of methylammonium and formamidinium in mixed cation perovskite: The optoelectronic and stability properties. *Nanotechnology* **2020**, *32*, 075406. [[CrossRef](#)]
22. Atourki, L.; Vega, E.; Mari, B.; Mollar, M.; Ahsaine, H.A.; Bouabid, K.; Ihlal, A. Role of the chemical substitution on the structural and luminescence properties of the mixed halide perovskite thin MAPbI_{3-x}Br_x (0 ≤ x ≤ 1) films. *Appl. Surf. Sci.* **2016**, *371*, 112–117. [[CrossRef](#)]
23. Tran, M.H.; Park, T.; Hur, J. Wide-bandgap CaSnO₃ perovskite as an efficient and selective deep-UV absorber for self-powered and high-performance pin photodetector. *ACS Appl. Mater. Interfaces* **2021**, *13*, 13372–13382. [[CrossRef](#)]
24. Liu, Y.; Yang, Z.; Cui, D.; Ren, X.; Sun, J.; Liu, X.; Zhang, J.; Wei, Q.; Fan, H.; Yu, F.; et al. Two-inch-sized perovskite CH₃NH₃PbX₃ (X = Cl, Br, I) crystals: Growth and characterization. *Adv. Mater.* **2015**, *8*, 5176–5183. [[CrossRef](#)]
25. Zhang, Z.; Zheng, W.; Lin, R.; Huang, F. High-sensitive and fast response to 255 nm deep-UV light of CH₃NH₃PbX₃ (X = Cl, Br, I) bulk crystals. *R. Soc. Open Sci.* **2018**, *5*, 180905. [[CrossRef](#)]
26. Nedelcu, G.; Protesescu, L.; Yakunin, S.; Bodnarchuk, M.I.; Grotevent, M.J.; Kovalenko, M.V. Fast anion-exchange in highly luminescent nanocrystals of cesium lead halide perovskites (CsPbX₃, X = Cl, Br, I). *Nano Lett.* **2015**, *15*, 5635–5640. [[CrossRef](#)]
27. Pellet, N.; Gao, P.; Gregori, G.; Yang, T.Y.; Nazeeruddin, M.K.; Maier, J.; Grätzel, M. Mixed-organic-cation Perovskite photovoltaics for enhanced solar-light harvesting. *Angew. Chem.* **2014**, *126*, 3215–3221. [[CrossRef](#)]
28. Singh, T.; Miyasaka, T. Stabilizing the efficiency beyond 20% with a mixed cation perovskite solar cell fabricated in ambient air under controlled humidity. *Adv. Energy Mater.* **2018**, *8*, 1700677. [[CrossRef](#)]
29. Zou, Y.; Zhang, Y.; Hu, Y.; Gu, H. Ultraviolet detectors based on wide bandgap semiconductor nanowire: A review. *Sensors* **2018**, *18*, 2072. [[CrossRef](#)]
30. Zeng, H.; Wu, Y.; Zhang, J.; Kuang, C.; Yue, M.; Zhou, S. Grain size-dependent electrical resistivity of bulk nanocrystalline Gd metals. *Prog. Nat. Sci. Mater. Int.* **2013**, *23*, 18–22. [[CrossRef](#)]

31. Ghods, S.; Esfandiari, A.; Irajizad, A.; Vardast, S. Enhanced Photoresponse and Wavelength Selectivity by SILAR-Coated Quantum Dots on Two-Dimensional WSe₂ Crystals. *ACS Omega* **2022**, *7*, 2091–2098. [[CrossRef](#)]
32. Nguyen, T.M.H.; Shin, S.G.; Choi, H.W.; Bark, C.W. Recent advances in self-powered and flexible UVC photodetectors. *Exploration* **2022**, *2*, 20210078. [[CrossRef](#)]
33. Wang, Z.; Clark, J.K.; Ho, Y.L.; Delaunay, J.J. Hot-electron photodetector with wavelength selectivity in near-infrared via Tamm plasmon. *Nanoscale* **2019**, *11*, 17407–17414. [[CrossRef](#)] [[PubMed](#)]
34. Kada, T.; Asahi, S.; Kaizu, T.; Harada, Y.; Tamaki, R.; Okada, Y.; Kita, T. Efficient two-step photocarrier generation in bias-controlled InAs/GaAs quantum dot superlattice intermediate-band solar cells. *Sci. Rep.* **2017**, *7*, 1–10. [[CrossRef](#)] [[PubMed](#)]
35. Nguyen, T.M.H.; Lee, S.K.; Kim, S.; Bark, C.W. Practical Demonstration of Deep-Ultraviolet Detection with Wearable and Self-Powered Halide Perovskite-Based Photodetector. *ACS Appl. Mater. Interfaces* **2021**, *13*, 57609–57618. [[CrossRef](#)] [[PubMed](#)]
36. Ji, Y.; Wang, M.; Yang, Z.; Qiu, H.; Ji, S.; Dou, J.; Gaponenko, N.V. Highly stable Na: CsPb (Br, I) ₃@ Al₂O₃ nanocomposites prepared by a pre-protection strategy. *Nanoscale* **2020**, *12*, 6403–6410. [[CrossRef](#)] [[PubMed](#)]
37. Yin, W.; Yang, J.; Zhao, K.; Cui, A.; Zhou, J.; Tian, W.; Li, W.; Hu, Z.; Chu, J. High responsivity and external quantum efficiency photodetectors based on solution-processed Ni-doped CuO films. *ACS Appl. Mater. Interfaces* **2020**, *12*, 11797–11805. [[CrossRef](#)]
38. Dou, L.; Yang, Y.M.; You, J.; Hong, Z.; Chang, W.H.; Li, G.; Yang, Y. Solution-processed hybrid perovskite photodetectors with high detectivity. *Nat. Commun.* **2014**, *5*, 1–6. [[CrossRef](#)]
39. Zhang, Z.X.; Li, C.; Lu, Y.; Tong, X.W.; Liang, F.X.; Zhao, X.Y.; Wu, D.; Xie, C.; Luo, L.B. Sensitive deep ultraviolet photodetector and image sensor composed of inorganic lead-free Cs₃Cu₂I₅ perovskite with wide bandgap. *J. Phys. Chem. Lett.* **2019**, *10*, 5343–5350. [[CrossRef](#)]
40. Zhang, Q.; Jie, J.; Diao, S.; Shao, Z.; Zhang, Q.; Wang, L.; Deng, W.; Hu, W.; Xia, H.; Yuan, X.; et al. Solution-processed graphene quantum dot deep-UV photodetectors. *ACS Nano* **2015**, *9*, 1561–1570. [[CrossRef](#)]
41. Chen, Y.C.; Lu, Y.J.; Lin, C.N.; Tian, Y.Z.; Gao, C.J.; Dong, L.; Shan, C.X. Self-powered diamond/ β -Ga₂O₃ photodetectors for solar-blind imaging. *J. Mater. Chem. C* **2018**, *6*, 5727–5732. [[CrossRef](#)]
42. Guo, D.; Liu, H.; Li, P.; Wu, Z.; Wang, S.; Cui, C.; Li, C.; Tang, W. Zero-power-consumption solar-blind photodetector based on β -Ga₂O₃/NSTO heterojunction. *ACS Appl. Mater. Interfaces* **2017**, *9*, 1619–1628. [[CrossRef](#)]
43. Zhao, B.; Wang, F.; Chen, H.; Zheng, L.; Su, L.; Zhao, D.; Fang, X. An ultrahigh responsivity (9.7 mA W⁻¹) self-powered solar-blind photodetector based on individual ZnO–Ga₂O₃ heterostructures. *Adv. Funct. Mater.* **2017**, *27*, 1700264. [[CrossRef](#)]

Disclaimer/Publisher’s Note: The statements, opinions and data contained in all publications are solely those of the individual author(s) and contributor(s) and not of MDPI and/or the editor(s). MDPI and/or the editor(s) disclaim responsibility for any injury to people or property resulting from any ideas, methods, instructions or products referred to in the content.